

Application of Multistage Drying Profiles for Accelerated Production of Li-Ion Battery Anodes Using Infrared Radiation: Validation with Electrochemical Performance and Structural Properties

Andreas Altvater,* Julian Klemens, Julian Borho, Anna Smith, Thilo Heckmann, Philip Scharfer, and Wilhelm Schabel

The drying of solvent-processed electrodes is a critical process step in the manufacturing of lithium-ion batteries. The technology used to introduce the energy required for drying into the material, combined with the specified process parameters, significantly influences the resulting electrode properties. A major challenge is to counteract binder migration effects that may occur during drying of the porous electrode structure, causing a decrease in adhesion and electrochemical performance, especially for high drying rates. From this motivation, investigations on the influence of process design during near-infrared drying of aqueous-processed graphite anodes are carried out. A multistage drying design with varying parameters in specific drying sections with energy input by radiation is applied. The results show that the specific application of a three-stage drying profile in combination with energy input by radiation enables a significant decrease in drying time by at least 60% while the electrode properties can be preserved. These findings indicate a beneficial development of binder distribution as a consequence of multistage NIR drying, evidenced by adhesion and electrochemical performance. Finally, the application of the multistage drying profile is theoretically transferred to an industrial-scale roll-to-roll dryer, whereby the necessary dryer length can be reduced by 53%.

1. Introduction


Electrode drying is a crucial and potentially limiting process step in the lithium-ion battery manufacturing chain.^[1] While the coating step for wet-processed electrodes can be performed at high coating speeds, the application of high drying rates (HDRs) poses a challenge to throughput in electrode production.^[2] In this context, high-energy demand on the one hand and process parameter-dependent electrode properties on the other hand require the need for an optimally controlled drying process.^[3,4] Various studies have demonstrated the significance of the drying process for the production costs of battery cells.^[3,5–7] Schünemann et al. attributed 45–57% of the total energy consumption to drying,^[5] while another study estimates that coating and drying make up a total of 21% of the battery cell production costs.^[6] Thomiczek et al. on the basis of various studies, assigned a share of 34–48% of the energy consumption of cell production

to the coating and drying process.^[7] With regard to the electrode properties, a process parameter-dependent development of these during drying is known.^[8] The adhesion strength between the electrode coating and the current collector foil, which decreases in particular at HDRs, can be mentioned as a representative indicator.^[9–13] In addition, the electrochemical performance of fast-dried electrodes deteriorates compared to gently dried electrodes due to the accumulation of insulating binder and carbon black at the surface, which leads to increased electrical resistance.^[9,14] Furthermore, an uneven distribution of components over the electrode height has been proven to adversely affect the ionic conductivity, which can additionally impair the capacity of electrodes.^[15,16]

In literature, binder migration is attributed to capillary pressure-induced initiation of concentration differences during depletion of the porous electrode structure, resulting in an inhomogeneous distribution of components.^[11] However, it has been shown that these effects can be compensated by selecting appropriate process parameters to a certain extent.

A. Altvater, J. Klemens, J. Borho, T. Heckmann, P. Scharfer, W. Schabel
Thin Film Technology (TFT)
Karlsruhe Institute of Technology (KIT)
Straße am Forum 7, Karlsruhe 76131, Germany
E-mail: andreas.altvater@kit.edu

A. Smith
Institute for Applied Materials (IAM)
Karlsruhe Institute of Technology (KIT)
Hermann-von-Helmholtz-Platz 1, 76344 Eggenstein-Leopoldshafen,
Germany

 The ORCID identification number(s) for the author(s) of this article can be found under <https://doi.org/10.1002/ente.202301272>.

© 2024 The Authors. Energy Technology published by Wiley-VCH GmbH. This is an open access article under the terms of the Creative Commons Attribution License, which permits use, distribution and reproduction in any medium, provided the original work is properly cited.

DOI: 10.1002/ente.202301272

Convective drying experiments with an isothermal process design, using a temperature-controlled plate and drying air regulated to the same temperature, as well as infrared (IR) drying experiments indicate that a high film temperature and a low convective heat transfer coefficient, corresponding to a low mass transfer coefficient, can have a positive effect on adhesion.^[12,17] The use of near-infrared (NIR) radiation also proved effective in overcoming film temperature limitations during drying and drying speed limitations, allowing the drying process to be conducted at higher throughput rates while maintaining or improving adhesion compared to a convective drying process.^[17] Although the throughput rate can be increased by the targeted application of NIR radiation, a tendency of decreasing adhesion with increasing drying rate is still observed for aqueous-processed graphite anodes.^[17]

Various other approaches to improve the efficiency and quality of the drying process are described in literature. Some studies reveal that the application of multilayer architecture electrodes with individually adapted binder proportions, particle sizes, shapes or particle porosities can counteract the effects of decreasing adhesion as well as decreasing capacities.^[18,19] Another promising approach to oppose low adhesion values is the use of primer coatings with high binder contents.^[2,20] Yet, a further concept that serves as the main basis for the study presented is the application of multistage drying profiles as introduced by Jaiser et al. which could be applied to achieve a time saving of about 40%.^[21] The concept is based on the hypothesis that structure formation and binder migration during drying take place in characteristic phases.^[9,21] To reveal the mechanisms responsible for migration of binder during drying, the authors performed drying experiments with graphite anodes using polyvinylidene fluoride (PVDF) binder dissolved in N-Methyl-2-pyrrolidone (NMP). Drying was carried out isothermally with simultaneous use of convection and a temperature-controlled plate in two stages, starting with a HDR \dot{m}_{HDR} of $1.2 \text{ g m}^{-2} \text{ s}^{-1}$ and switching to a low drying rate (LDR) \dot{m}_{LDR} of $0.5 \text{ g m}^{-2} \text{ s}^{-1}$ by adjusting the volume flow of the drying air at defined transition times.^[9] The results of this study on electrode adhesion and fluorine concentration at the electrode's bottom side, representing the PVDF binder, as a function of transition time are shown in **Figure 1**.

The authors found that adhesion strength develops proportionally to the fluorine concentration near the current collector. Consequently, adhesion strength and binder migration are closely related and thus, adhesion was defined an appropriate measure of microstructure homogeneity with respect to additive distribution. The decrease of adhesion strength with increasing drying rate was attributed to binder migration which is more pronounced for HDR than for LDR. Moreover, the adhesion was found to decrease as a function of transition time, although a time interval at the beginning of drying was not affected by the HDR. The time at the end of this interval was identified as the first characteristic time $t_{c,1}$. A similar section of constant adhesion despite the application of HDR was observed at a later state in the drying process, the time of transition was designated as $t_{c,2}$. The interval between $t_{c,1}$ and $t_{c,2}$ was consequently defined as characteristic for the structure formation during drying. Nevertheless, binder accumulation was already observed

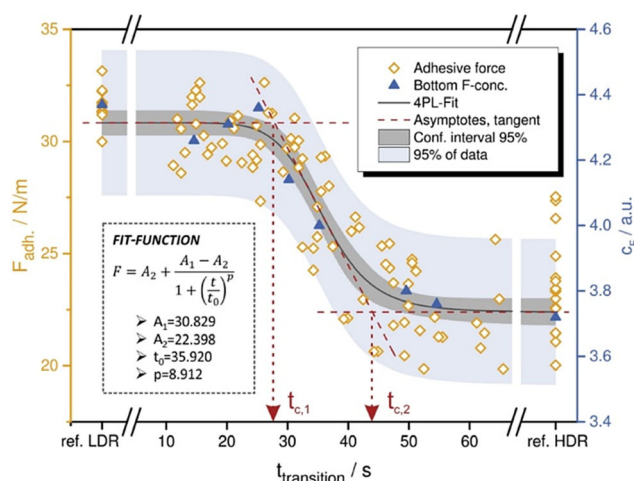


Figure 1. Development of adhesion strength and fluorine concentration at the bottom of the electrode versus the transition time compared to reference samples (LDR and HDR). The statistics are based on a four-parameter logistic (4PL) regression. The characteristic transition times are estimated by intersecting asymptotes and a tangent drawn to the inflection point. Reproduced with permission.^[9] Copyright 2017, Elsevier.

immediately after the start of drying at the electrode top surface (also by fluorine concentration measurements) under rapid drying conditions, despite a plateau being expected, since capillary forces are not yet acting at the beginning of drying. Again, a plateau of constant binder concentration at the top surface appeared after exceeding $t_{c,2}$.^[9]

From the discussed mechanisms and further findings, an abstracted concept for the drying process emerged. A schematic representation of the drying process and the various phases occurring is correspondingly shown in **Figure 2**.

After coating, shrinkage of the film initiates due to solvent evaporation at the beginning of the drying process (Figure 2a,b). The electrode coating dries in a purely gas-phase-controlled manner and thereby exhibits the behavior of a film of pure liquid that evaporates at its surface. When the final porosity is reached, the film shrinkage process is completed and ideally, the solvent further saturates the capillary network (Figure 2c). As drying progresses, pore emptying initiates, and the pores empty depending on their dimensions according to the Young–Laplace equation.^[22,23] Consequently, larger pores empty first, while smaller pores remain filled (Figure 2d). Even after film shrinkage terminates, drying continues with a constant drying rate due to pronounced capillary transport processes.^[12,24,25] Prior to thorough drying, individual liquid clusters within the electrode structure may be isolated from capillary transport causing them to evaporate in place with additional mass transfer resistance before the dry electrode layer is established (Figure 2e).

According to the results discussed with respect to Figure 1, the critical intervals during drying were assigned to the associated mechanisms. Binder migration was consequentially found to be caused by capillary transport during pore emptying. Accordingly, the first characteristic time $t_{c,1}$ coincides with the beginning of pore emptying, which for the parameters used in the study shown also corresponded to the end of film

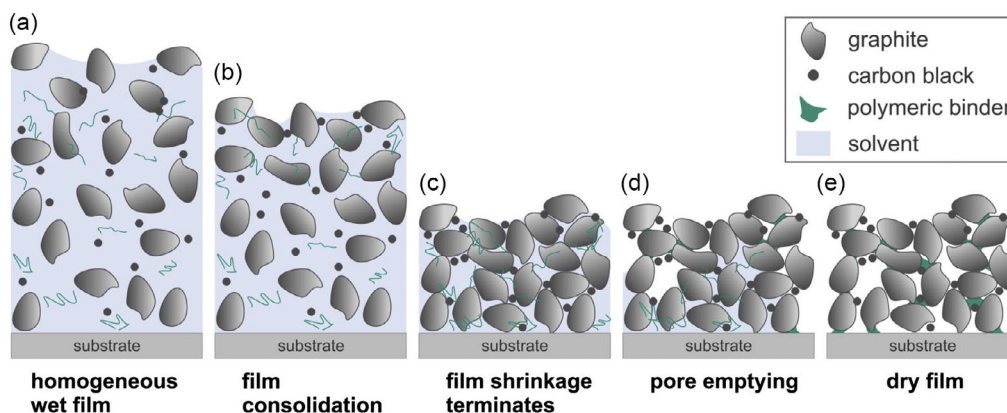


Figure 2. Schematic illustration of the drying of a particulate electrode film. a) At the beginning of drying after coating. b) During drying, the film shrinks due to solvent evaporation and the particles approach each other until the final porosity c) is reached. d) Pore emptying and capillary transport. e) Dry electrode. Reproduced with permission.^[24] Copyright 2017, Elsevier.

shrinkage t_{EoFS} .^[24] A theoretical value for t_{EoFS} can be estimated using the initial solvent loading $X_{\text{S},0}$, the density of the solvent ρ_{S} , the thickness h_{El} and the area weight m_{El} of the dry electrode, and the drying rate \dot{m}_{S} with Equation (1):^[14]

$$t_{\text{EoFS}} = \left(X_{\text{S},0} - \frac{\rho_{\text{S}} \varepsilon_{\text{El}} h_{\text{El}}}{m_{\text{El}}} \right) \frac{m_{\text{El}}}{\dot{m}_{\text{S}}} \quad (1)$$

Therefore, the volume fraction of solvent $\varphi_{\text{S}}(t_{\text{c},i})$ at $t_{\text{c},1}$ corresponds to the porosity ε_{El} of the dry electrode layer. This consideration is valid as long as the pores remain completely saturated with solvent during the shrinkage process and the absorption of solvents by graphite, carbon black, or binders remains unconsidered.^[9]

Nonetheless, previous studies indicate that the onset of pore depletion and the end of film shrinkage may not always coincide.^[8,25] Jaiser et al. found the onset of the critical phase in terms of binder migration to precede the end of film shrinkage significantly for small spherical active material particles as well as for increased drying rates.^[8]

The cited findings regarding the positive effect of a multistage drying design have to date been demonstrated in such systematic manner exclusively for solvent-based material systems, one specific process variant and, compared to the current state-of-the-art, substandard drying rates for high drying rate and low drying rates.

To attain minimal drying times in the respective drying sections, additional or alternative energy input methods are required. The suitability of NIR radiation for the achievement of HDRs with acceptable electrode properties has been demonstrated in a previous work.^[17] Within the aim of reducing production costs of battery electrode manufacturing and increasing throughput, the combined application of multistage drying profiles and heat input by infrared radiation is thus a highly feasible approach, particularly for aqueous-processed electrodes, due to the high evaporation enthalpy of water. With the aim of a tailored process in terms of throughput and electrode properties, the three-stage model is adapted to industrially relevant drying rates and a water-based anode slurry using a carboxymethyl cellulose (CMC) and styrene-butadiene-rubber (SBR) binder system in this

study. CMC/SBR generally shows good absorption to the active material while PVDF mainly increases matrix viscosity with poor affinity to graphite and carbon black.^[26,27] In addition, the temperature stability of the main binder SBR qualifies it for use in a drying scenario with heat input by radiation, involving comparatively high electrode temperatures during drying.^[26]

To achieve this, it is first necessary to verify whether the identified mechanisms that justify the multistage model are applicable to the present material system and energy input with NIR radiation. The achievable average drying rates are subsequently discussed and electrochemical characterization of the electrodes produced using the multistage processes is performed before the method is theoretically scaled up to a production line.

2. Multistage Near-Infrared Drying

To experimentally determine the critical phases during drying, NIR drying was first performed in two-stage transition experiments and the influence of transition times and drying rates on electrode adhesion, as a representative electrode quality indicator, was evaluated. Based on the results, the procedure was extended to a three-stage model, and its applicability classified based on achievable average drying rates and electrode adhesion. Furthermore, the dried electrodes were characterized in full-cell tests regarding their electrochemical performance. For all experimental investigations with subsequent electrode characterization, electrodes with a dry areal mass loading m_{El} of $\approx 130 \text{ g m}^{-2}$ ($\approx 4.4 \text{ mAh cm}^{-2}$), a thickness h_{El} of $\approx 140 \mu\text{m}$, and a porosity ε_{El} of ≈ 0.56 were produced from the slurry described in the experimental section. For multistage drying experiments, the HDR \dot{m}_{HDR} was adjusted to $6 \text{ g m}^{-2} \text{ s}^{-1}$, while the low drying rates \dot{m}_{LDR} was regulated to $0.75 \text{ g m}^{-2} \text{ s}^{-1}$.

2.1. Evaluation of Critical Drying Intervals

In this section, the evaluation of property-determining intervals during drying using two-stage and three-stage drying experiments is discussed. From two-stage drying experiments with

subsequent adhesion measurement, the first and second critical transition times ($t_{c,1}$ and $t_{c,2}$) can be determined by adjusting the drying rate from HDR to LDR at different times during the drying process. The drying rate is controlled by the applied heat input of the used NIR radiator. The required power settings for HDR and LDR were evaluated in preceding calibration tests gravimetrically as described in a previous study.^[17] Afterwards, the dried electrodes were characterized in terms of adhesion.

2.1.1. Two-Stage Drying Experiments

Figure 3 shows the adhesion strength data for two-stage dried graphite anodes as a function of the transition time, the point of time at which the drying rate was switched from HDR to LDR. The data shown represents electrodes produced with transition times $t_{trans,1}$ between 3.6 and 30.8 s.

In general, the data show that the adhesion strength development is strongly dependent on the process control, in this particular case the transition time. Up to a certain transition time, the adhesion strength is constant within the error bars, followed by a period with a strongly decreasing adhesion strength as the transition time increases. This steeply decreasing curve flattens out again after a certain transition time, whereupon a period with an approximately constant adhesion strength reappears. The comparison with literature permits conclusion that the course of the adhesion strength values along the transition time corresponds qualitatively to the course observed by Jaiser et al.^[9] In literature, the tripartite course of drying emerging from transition experiments is explained as follows: at the onset of drying, additives are homogeneously distributed within the drying

electrode film. Due to the uniform distribution and the homogeneous solvent removal, the adhesion strength during shrinkage (reduction of film thickness) is not influenced by the drying rate. When the end of film shrinkage is reached, pore emptying and capillary-driven solvent transport initiate, involving binder migration, whose impact on adhesion strength strongly depends on the prevailing drying rate.^[9,12,24] The second plateau is assumed to be due to the breakdown of capillary connections within the electrode pore network, resulting in the termination of capillary binder transport. Liquid may still be present in liquid clusters in individual pores without a continuous capillary network and thus, no capillary pathway is present that could enable binder migration.^[14] From this point on, the adhesion strength of the electrode and the concentration of binder at the interface between substrate and active material is constant and unaffected by the prevailing drying rate.

The qualitative course of the data developed in this study shows a predominantly consistent alignment with the described mechanisms. For a more precise classification, the critical transition times need to be extracted. Therefore, a fit function, which is noted in the experimental section, can be applied to transiently map the course of the adhesion strength as a function of the transition time. The 4PL regression is plotted and shows good agreement with the measured data. The evaluated fit parameters are listed in the Table S2, Supporting Information. The asymptotic tails of the fit function represent the plateaus for early and late transition times and correspond to the respective reference adhesion strengths for single-stage drying within the limits of measurement accuracy. These were determined for single-stage drying at LDR to $12.6 \pm 0.3 \text{ N m}^{-1}$ and for single-stage drying at HDR to $2.4 \pm 0.1 \text{ N m}^{-1}$. Critical points of time are indicated in the diagram as $t_{c,1}$ and $t_{c,2}$ and can be determined by means of the intersection of the respective asymptotes and the tangent line. For the specified material and process parameters, $t_{c,1}$ is located at a drying time with HDR of 11.6 s and $t_{c,2}$ at 19.9 s. Although Figure 3 enables the identification of a characteristic drying phase, offering initial insights into the drying process, it does not address the mechanisms governing the film's structure formation. To enhance comprehension, the characteristic transition times are converted into a volumetric quantity, yielding a more illustrative depiction of the film's state at the time of the change of drying rate. The critical solvent volume fractions $\varphi_S(t_{c,i})$ that are present at the beginning and at the end of the critical structure-determining interval can be identified by applying Equation (2)–(4):^[21]

$$X_S(t) = X_{S,0} - \frac{\dot{m}_{\text{HDR}}}{m_{\text{El}}} t \quad (2)$$

$$x_S(t) = \frac{X_S(t)}{1 + X_S(t)} \quad (3)$$

$$\varphi_S(t) = \frac{x_S(t)}{(1 - x_S(t)) \frac{\rho_S}{\rho_{\text{El}}} + x_S(t)} \quad (4)$$

$X_{S,0}$ represents the initial solvent loading, which was individually determined for the slurry after the mixing step (see Supporting Information), while $x_S(t)$ describes the mass fraction of solvent at the respective points of time. ρ_S describes the

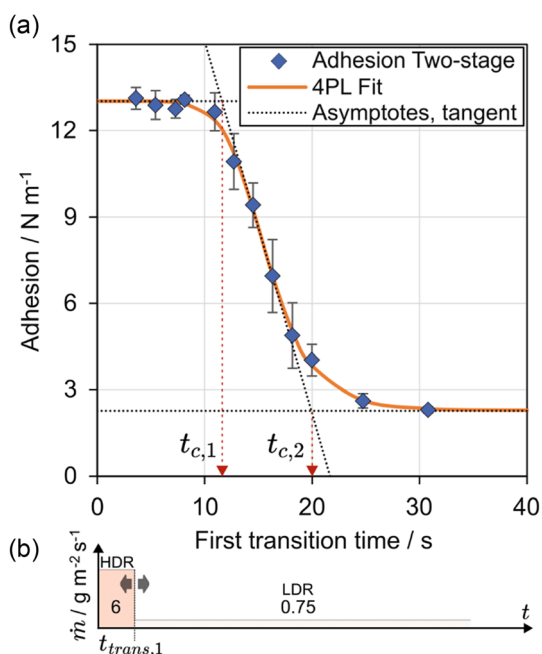


Figure 3. a) Adhesion as a function of the first transition time $t_{trans,1}$ for two-stage NIR drying of aqueous-processed graphite anodes. Measurement data are fitted with a 4PL regression. b) Schematic illustration of the approach of two-stage transition experiments.

Table 1. Drying rates, material systems, drying methods, material and critical process parameters examined from experimental data of this study and the study by Jaiser et al.

Source of data	HDR LDR [$\text{g m}^{-2} \text{s}^{-1}$]	Material system	Drying method	m_{El} [g m^{-2}]	ϵ_{El} [-]	$\varphi_{\text{S}}(t_{\text{c},1})$ [-]	$\varphi_{\text{S}}(t_{\text{c},2})$ [-]
This study	6 0.75	Graphite ($d_{50} = 18.4 \mu\text{m}$)	Near-infrared + Free convection	130	0.56	0.61	0.43
		Carbon black					
		CMC/SBR					
Data from Jaiser et al. ^[9]	1.19 0.52	Water					
		Graphite ($d_{50} = 20.4 \mu\text{m}$)	Convection + Conduction (isothermal)	70.5	0.59	0.58	0.44
		Carbon black					
		PVDF					
		NMP					

density of the used solvent water and $\bar{\rho}_{\text{El}}$ represents the averaged density of solid components in the electrode (see Table S1, Supporting Information). For application of the calculation method, it must be assumed that the drying rate is present from the very beginning of the experiment and remains constant during the respective phase. The results for the critical solvent volume fractions are listed in **Table 1**. As a reference, the data from literature are given as well as the porosity ϵ_{El} of the electrodes.

For the material system in this study, critical solvent contents $\varphi_{\text{S}}(t_{\text{c},1})$ of 61 vol% at $t_{\text{c},1}$ and $\varphi_{\text{S}}(t_{\text{c},2})$ of 43 vol% at $t_{\text{c},2}$ can be identified. As a reference value for the classification of the first critical solvent content, the porosity of the layers is used. Jaiser et al. showed that for their material system, the solvent volume fraction at the end of film shrinkage approximately matches the porosity of the dry electrode and concluded, that once the final porosity is reached, adhesion affecting binder migration initiates.^[8] For the data compiled here, the critical solvent content $\varphi_{\text{S}}(t_{\text{c},1})$ is slightly higher than the porosity. Interestingly, literature reports that at higher drying rates the first critical point of time, may also occur well before the termination of film shrinkage.^[8] Given a drying rate of $6 \text{ g m}^{-2} \text{ s}^{-1}$, this condition is clearly met, especially considering that the abovementioned reference investigated drying rates of only $1.8 \text{ g m}^{-2} \text{ s}^{-1}$, suggesting that similar mechanisms may be involved. A potential explanation for the initiation of the critical interval before reaching the final porosity lies in the possibility of pore emptying, which is accompanied by binder migration, starting before the film shrinkage is entirely finished, whereby this hypothesis does not appear reasonable from a mechanistic point of view. The results could also suggest an inhomogeneous binder distribution occurring prior to the end of film shrinkage regardless of pore emptying mechanisms extending to the substrate due to a HDR. At an early drying stage, a concentration gradient could form, as demonstrated for PVDF/NMP electrodes, while premature pore drainage at the surface, which could trigger binder migration, is possible likewise.^[14,24] Comparable observations have not yet been made for the CMC/SBR binder system, however. Although a final breakdown of the underlying mechanisms cannot be provided, the critical drying interval, in which adhesion-reducing effects occur, appears prior to the final film porosity being reached when infrared drying is carried out with the specified process and material parameters.

Apart from the references consulted for comparison, the results also qualitatively align with investigations at other research institutions. Fink et al. investigated the drying of graphite anodes and used a two-stage concept in which part of the solvent was first dried from an initial 60 wt% to 33–36 wt% using a combination of laser radiation and convection at a high drying rate. The authors found no systematic correlation between an increased drying rate at the beginning of drying and a deterioration of properties. The findings were also quantified on the basis of adhesive strength where values comparable to those of a convective reference process could be achieved. However, cracks occurred at very high drying rates in their investigations, which were conducted on electrode layers of 60–70 μm thickness.^[28] The two-stage drying process incorporating NIR radiation and convection also was empirically investigated by Wolf et al. for LFP cathodes using an edge-emitting diode laser system. The study focused on an LFP slurry with an initial solvent content of 54 wt% and a wet film thickness of 160 μm . The authors achieved a significant reduction in drying time of up to 63% with comparable electrode quality compared to conventional convection drying in a single-stage design, by employing higher drying rates through the application of radiation in the initial stage of drying. The results were substantiated by means of adhesion, electrical conductivity, and c-rate tests in half-cell configuration.^[29]

2.1.2. Three-Stage Drying Experiments

The two-stage drying tests have shown that the negative influence of high drying rates only occurs between $\varphi_{\text{S}}(t_{\text{c},1})$ and $\varphi_{\text{S}}(t_{\text{c},2})$. However, since the determination of $t_{\text{c},1}$ with the two-stage method requires drying with HDR in an interval that exceeds the uncritical region, the second critical point of time $t_{\text{c},2}$ was additionally verified by a further series of experiments. Those were carried out with a fixed first transition time $t_{\text{trans},1}$ from HDR to LDR while the second transition time from LDR to HDR $t_{\text{trans},2}$ was varied. The first transition time was set to $t_{\text{trans},1} = 10 \text{ s}$, to be within the identified noncritical drying interval prior to the critical transition time $t_{\text{c},1}$ (11.6 s, compare Figure 3a), while the second transition time was varied between 50.7 and 95.2 s of the total drying time. According to Equation (4), the solvent volume fraction at the first transition

point is about 0.65, which is significantly higher than the evaluated critical volume fraction of 0.61. To compare the experimental data obtained with this method with the two-stage tests shown in Figure 3, the second critical time for three-stage drying $t_{c,2,calc}$ was calculated from the critical loadings $X_S(t_{trans,1})$ and $X_S(t_{c,2})$ with Equation (5). The associated critical solvent volume fractions are listed in Table 1:

$$t_{c,2,calc} = t_{trans,1} + (X_S(t_{trans,1}) - X_S(t_{c,2})) \frac{m_{El}}{m_{LDR}} \quad (5)$$

The results for the adhesion strength of the electrodes are plotted as a function of the second transition time in Figure 4.

The adhesion strength determined for all dried electrodes is within the adhesion strength range between the references for single-stage drying at LDR and HDR, if the second transition to HDR was executed before reaching the calculated second transition time. Furthermore, an approximately linear increase of adhesion strength with increasing transition time can be observed. According to the hypothesis of this study, the adhesion values in this interval are reduced because the transition to HDR was performed too early, i.e., still in the process interval in which an increased drying rate leads to increased binder migration and correspondingly lower adhesion. Consequently, the evaluation of the critical drying intervals with the two-stage drying method can be validated to a considerable extent on the basis of the three-stage dried electrodes. Furthermore, it can be observed that the data point of adhesion at the highest selected transition time is slightly above the measured value for single-stage gently dried electrodes (LDR). An increased adhesion could also be due to a positive effect of the increased film temperature caused by the

high power input in the final drying phase, since in previous studies a positive effect of high temperature in single-stage drying experiments was demonstrated.^[12,16,17] However, it is not yet clear in which interval during the drying process the effect comes into play in terms of structure formation, which may be a relevant question for future research. An ultimate explanation for the existence of a second, noncritical interval at high drying rates, supported by experimental results, is not found in the literature either. A reasonable interpretation is the collapse of the capillary network, which can occur when the pores empty according to their size distribution and the associated capillary pressure. As a result, larger pores empty faster than smaller ones, leading to isolated liquid clusters instead of a continuous capillary network at a certain point of time during the drying process. Consequently, there can be no global solvent transport, carrying the binder from the interface between electrode material and current collector to the electrode surface, which may worsen adhesion.^[9]

2.2. Process Design and Drying Time

The savings potential with regard to drying time or dryer length for single-, two- and three-stage drying processes can be calculated by using the average drying rate of the respective drying profile. The average or overall drying rate \dot{m}_{avg} includes the dwell time in the LDR mode t_{LDR} and HDR mode t_{HDR} (see Table S3, Supporting Information) as well as the absolute drying time $t_{dry,abs}$ and is calculated according to Equation (6):

$$\dot{m}_{avg} = \frac{\dot{m}_{HDR}t_{HDR} + \dot{m}_{LDR}t_{LDR}}{t_{dry,abs}} \quad (6)$$

For a drying process carried out exclusively in LDR mode, \dot{m}_{avg} corresponds to \dot{m}_{LDR} while for HDR only mode \dot{m}_{avg} equals \dot{m}_{HDR} . The adhesion strength values of the experiments shown in Figure 3 and 4 are displayed over the calculated average drying rates in Figure 5a. The specified drying rates for LDR ($0.75 \text{ g m}^{-2} \text{ s}^{-1}$) and HDR ($6 \text{ g m}^{-2} \text{ s}^{-1}$) were used for the calculation, while the drying times t_{HDR} , t_{LDR} and $t_{dry,abs}$ were extracted from the drying curves.

The results show that with both, two-stage and three-stage drying processes, an increase in the average drying rate with at least the same adhesion strength compared to a gentle, single-stage drying process (LDR) can be achieved for a graphite anode. For the electrodes showing at least a similar adhesion as the reference sample (LDR, $0.75 \text{ g m}^{-2} \text{ s}^{-1}$), an increase in drying rate to $1.04 \text{ g m}^{-2} \text{ s}^{-1}$ (+39%) for the two-stage process and $1.86 \text{ g m}^{-2} \text{ s}^{-1}$ (+147%) for the three-stage process can be found. However, it is also evident that in multistage processes, a low adhesion level, which corresponds to the reference drying rate for single-stage drying at a higher drying rate is possibly reached at lower overall drying rates than in a single-stage process, which is the case if the transition times are not optimally selected according to the critical transition times. As a result, adhesion will decrease sharply with increasing dwell time when a HDR is applied in the critical drying interval. A comparison of the data points for two-stage drying at an average drying rate of 2.3 and $4.4 \text{ g m}^{-2} \text{ s}^{-1}$ with the reference electrode for single-stage drying

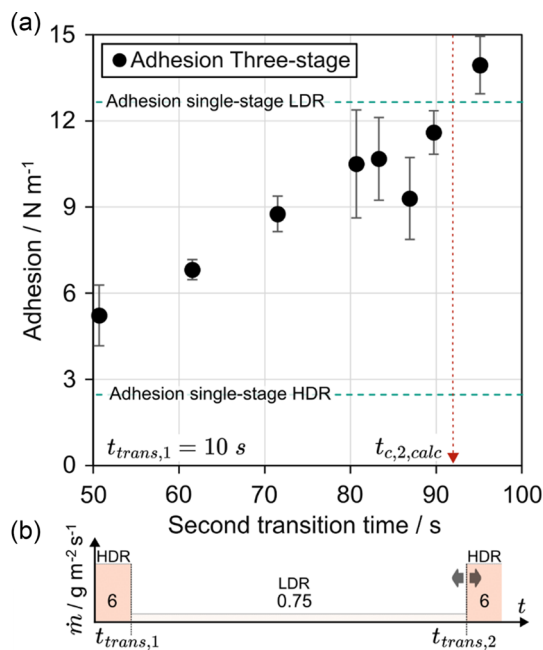


Figure 4. a) Adhesion strength as a function of the second transition time for three-stage NIR drying of aqueous-processed graphite anodes. The reference values for drying exclusively at LDR and HDR are plotted as horizontals. b) Schematic illustration of the approach of three-stage transition experiments.

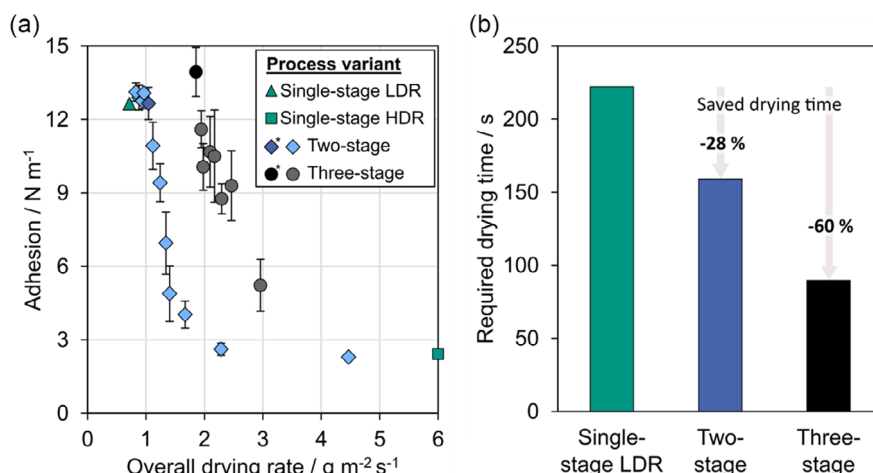


Figure 5. a) Adhesion strength as a function of the overall drying rate \dot{m}_{avg} for different process variants: single-, two- (HDR \rightarrow LDR), and three-stage drying (HDR \rightarrow LDR \rightarrow HDR) of graphite anodes with a dry area weight of 130 g m^{-2} . The * marked data points represent the multistage dried electrodes with an adhesion of at least the value of single-stage LDR dried electrode with the maximal possible overall drying rate used for (b). b) Drying times determined from the calculated average drying rates in (a) for the process variants while maintaining at least the adhesion strength of the single-stage LDR reference. The time savings for the multistage processes are given as percentages.

at HDR demonstrates this aspect. These data confirm the fact that only the critical interval during drying (between $\varphi_S(t_{c,1})$ and $\varphi_S(t_{c,2})$) is property-determining with regard to adhesion.

Figure 5b illustrates the drying times calculated from the average drying rates for the electrodes of the respective process variants with the highest possible overall drying rate from Figure 5a, providing at least the adhesion strength of the single-stage LDR reference electrode. For the two-stage process, the electrode at an average drying rate of $1.04 \text{ g m}^{-2} \text{ s}^{-1}$ is relevant, for the three-stage process at $1.86 \text{ g m}^{-2} \text{ s}^{-1}$. Consequently, the appropriate application of a two-stage process with the specified drying rates reduces the drying time required for a graphite anode with 57 wt% solvent content and a dry areal loading of 130 g m^{-2} from 222 to 159 s (−28%) without a reduction of adhesion being accompanied. In the three-stage process, the drying time required is 89 s (−60%).

3. Electrochemical Characterization

To validate the multistage NIR drying concepts with regard to electrochemical performance, anodes dried with the different process variations (compare Section 2) were characterized electrochemically. The single-stage processed electrodes with drying rates of 0.75 and $6 \text{ g m}^{-2} \text{ s}^{-1}$ were investigated as references for LDR and HDR. To adjust the respective drying rates, the same power settings as for the investigations in Section 2 were used. For the two- and three-stage-processed electrodes, the transition times were chosen to be clearly within the range before reaching the critical volume fraction $\varphi_S(t_{c,1})$ and after $\varphi_S(t_{c,2})$, respectively. Accordingly, the first transition time from HDR to LDR, $t_{\text{trans},1}$ was set to 10 s, while the second transition time $t_{\text{trans},2}$ was set to 100 s. The corresponding solvent fractions calculated with Equation (4) as well as the drying settings for each process variant are listed in Table 2.

Table 2. Process variants, drying rates, and solvent volume fractions at the point of transition applied in the processing of the graphite anodes used for electrochemical characterization.

Process variant	Adjusted drying rate [$\text{g m}^{-2} \text{ s}^{-1}$]			Solvent fraction (vol.) @ $t_{\text{trans},i}$ [–]	
	1 st stage	2 nd stage	3 rd stage	$\varphi_S(t_{\text{trans},1})$	$\varphi_S(t_{\text{trans},2})$
Single-stage LDR	0.75	–	–	–	–
Single-stage HDR	6	–	–	–	–
Two-stage	6	0.75	–	0.65	–
Three-stage	6	0.75	6	0.65	0.42

Initially, two coin cells were built in a half-cell configuration with lithium as the counter electrode, for single-stage LDR and single-stage HDR processed electrodes, as these were expected to represent the most significant differences based on the adhesion results. Applying a c-rate of C/50 during formation of the coin cells, specific capacities of $365\text{--}370 \text{ mAh g}^{-1}$ were obtained for all graphite electrodes, which is close to the theoretical capacity of the active material graphite, although some of the measured capacity should be assigned to irreversible solid electrolyte inter-phase formation.^[30] Accordingly, full capacity is available and no differences in voltage potentials independent of the drying rate of the graphite electrodes are obtained. Further cycling of LDR and HDR at C/10, however, indicated capacity degradation, so that any performance testing, e.g., rate capability tests, seemed inappropriate in the coin-cell configuration. The formation voltage curves for the half-cells against specific capacity are shown in Figure S1, Supporting Information. According to literature, electrodes with a high area weight tend to show severe capacity degradation within half-cells upon cycling.^[31] The reason for insufficient capacity retention even at the same c-rate might be massive lithium plating and with that rapid ageing of the

cell.^[30] Nevertheless, the results from cell formation allowed to determine the areal capacity of the graphite electrodes to be $\approx 4.4 \text{ mAh cm}^{-2}$. Such high loading of electrodes depicts the state-of-the-art automotive application and thus it is highly relevant to study the behavior of high energy, thick electrodes.^[32]

To obtain any performance insights correlated to the drying process, pouch-type full cells were built using commercial NCM811 cathodes with a loading of $\approx 4.0 \text{ mAh cm}^{-2}$ for all four process variants according to the procedure described in the experimental section. The discharge capacity after formation (last cycle of four C/10 discharge/charge cycles) was $104 \pm 1 \text{ mAh}$ for all cells (compare Table S4, Supporting Information). The voltage curve during formation is shown in Figure S2, Supporting Information, for all tested pouch cells. To further investigate any electrochemical performance differences of the graphite anodes, all pouch cells were subject to an asymmetric rate test in discharge direction (to prevent any lithium plating and thus cell degradation, as likely during high c-rates^[33]). The results for the relative discharge capacity, normalized to the initial C/2 discharge capacity, for each cell of the different drying scenarios are shown in **Figure 6**. Thereby, the initial absolute capacities of all measured cells are nearly identical (compare Figure S3, Supporting Information).

The first observation to be made is that both cells of the same drying scenario show highly comparable values for relative capacity at the respective c-rates and trends, which testifies to the reproducibility of the selected pouch cell format. The relative discharge capacity shows significantly decreasing values for increasing c-rates for all tested cells. Highly loaded electrodes are used in high-energy applications, and, despite their high-energy density, naturally show rather poor power density. In fact, the capacity retention of similarly loaded commercial multilayer pouch cells (78 Ah) drops to less than 50% from 1 to 2C, while only $\approx 20\%$ of the initial capacity is accessible at 3C.^[34] Further, the electrodes studied were not calendered to enable the observation of the influence of the drying process isolated from other

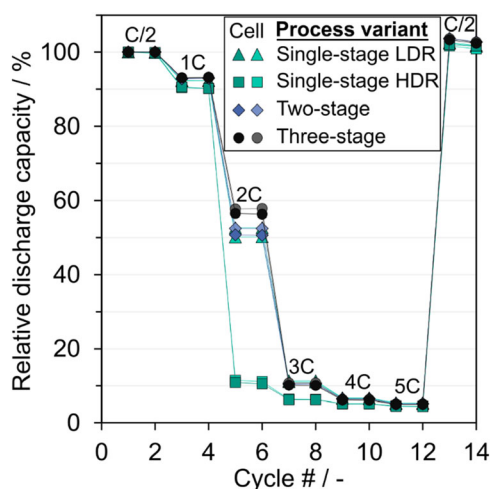


Figure 6. Rate-dependent relative discharge capacities of pouch cells built with noncalendered graphite anodes ($\approx 4.4 \text{ mAh cm}^{-2}$) dried using NIR in different process variants and commercial NMC811 cathodes ($\approx 4.0 \text{ mAh cm}^{-2}$).

process steps. Since porosity has a significant effect on the discharge process, noncalendered electrodes generally exhibit significantly higher capacitance retention as a consequence of lower resulting conductivity than calendered electrodes.^[11,35] At C/2, the capacity of the cells after cycling at high c-rates is in the same range as the capacity of the cells before. Thus, the loss of capacity is reversible and not due to degradation of the cells, but probably to an increase in reversible charge transfer limitations. For the single-stage gentle drying process (single-stage LDR), for example, the cells lose about 8% discharge capacity at 1C compared to C/2, for 2C the reduction amounts to 49% while for 3C 89% of the capacity at C/2 cannot be accessed. It is noticeable that the change in discharge capacity differs partly for the different process variants during anode drying. It was found that cells in which the electrodes were gently dried in a single-step LDR process performed significantly better than cells in which the drying rate was increased (single-stage HDR). While the capacity of the fast and slow-dried electrodes for a discharge rate of C/2 and 1C show comparable values, the difference in discharge capacity between LDR and HDR at 2C is $\approx 78\%$. Still, at 3C, the single-stage slow-dried electrodes also show severe discharge limitation, whereby their capacity reduces. Nevertheless, the fast-dried electrodes perform $\approx 43\%$ worse. This can be due to an increase in resistance, caused in large part by a nonuniform distribution of components due to binder migration, affecting the potential profile and discharge capacity at higher rates.^[9,11,13,18] A reduction in the discharge capacity can be caused by both increased electrical or ionic resistance. However, from the available data, it is not possible to determine conclusively which mechanism is primarily responsible for the loss of capacity, as this is not the focus of this study.

The observed characteristic is consistent with the results for the adhesion strength (compare Figure 3), the values of which allow to some extent a conclusion to be drawn regarding the component distribution in terms of binder content across the electrode height and specifically the amount of binder between the active material layer and the current collector foil.

Besides the single-stage dried electrodes, the discharge capacities of the cells with two- and three-stage dried electrodes were analyzed. The capacities of the two-stage dried electrodes match those of the electrodes dried at LDR in single-stage mode almost without deviation for all cycles. This is also in line with expectations, since the results on adhesion for properly conducted multistage drying do not indicate any microstructural changes that would affect the properties negatively. Consequently, a high drying rate in the first stage has no negative effect on adhesion or electrochemical performance. This is partwise in contrast to the study by Jaiser et al. who showed that binder accumulation at the electrode's surface for PVDF/NMP anodes in a convective process starts from the very beginning of drying, which potentially could lead to an increase in resistance and thus to decreased discharge capacities.^[9] Whether comparable effects are present for the drying processes and electrodes investigated here cannot be conclusively determined, a negative influence is at any rate not discernible. The cells with the anodes produced in a three-stage process show a similar behavior for the most part. Likewise, the expectation of no property degradation is met, since gentle drying (with LDR) was applied in the critical structure-determining drying step. However, it is noticeable that the discharge capacity for

three-stage dried electrodes at a discharge rate of 2C is even 11% higher than for the single-stage reference and the two-stage dried electrodes. This is also consistent with the results on adhesion: the three-stage dried electrode shows a slightly increased adhesion compared to the single-stage LDR reference and the two-stage dried electrode (compare Figure 5a). One possible explanation would be a positive influence of the increased temperature in the final drying stage, in which a high drying rate, i.e., a high-energy input, is applied, since a previous study on single-stage infrared drying of anodes demonstrated a positive impact of high temperature on adhesion during the drying process.^[17] For fast-dried hard carbon electrodes, a positive effect of electrode temperature during drying was found not only for adhesion but also for ionic conductivity, although the mechanisms ultimately responsible were not conclusively clarified.^[16] More profound interpretations are not advisable due to the limited data available, even though both factors, the improvement in adhesion as well as the discharge capacity, provide sufficient reason for further research. In conclusion, the data obtained on the electrochemical performance strongly support the hypothesis of this study and demonstrate that a significantly accelerated drying process is possible without causing a deterioration of microstructural or electrochemical properties using properly applied multistage drying profiles. Nevertheless, the ultimate performance of calendared electrodes dried in multiple stages with NIR remains an outstanding concern and poses a relevant subject for future research.

4. Theoretical Scale-up of Multistage Drying Concepts to Production Scale

With the aim of maximizing throughput in an industrially relevant production scenario, this section theoretically scales up the procedure to higher drying rates. For this purpose, the mechanisms shown are assumed to be applicable also for even higher drying rates with regard to critical transition times. In addition, heating and cooling times as well as run-in effects are neglected for the following considerations, while it is assumed that the entire drying process takes place without the influence of film-side drying resistances, which are only likely to occur with very thick electrodes.^[25] The deviations to be expected with regard to drying times as a result of the influences mentioned are estimated to be minor overall and quantitatively negligible. The maximum savings potentials for a higher drying rate of $10 \text{ g m}^{-2} \text{ s}^{-1}$ in the first and last drying section and a lower drying rate of $2.5 \text{ g m}^{-2} \text{ s}^{-1}$ in the middle drying section are discussed for the example of the drying of graphite anodes with an areal loading of 130 g m^{-2} ($\approx 4.4 \text{ mAh cm}^{-2}$) and an initial solvent content of 57 wt%. As shown in Section 2, the electrode properties influenced by the drying process are expected to be determined only in the critical drying interval between $\varphi_S(t_{c,1})$ and $\varphi_S(t_{c,2})$. The establishment of an increased drying rate for LDR in the critical interval, as considered here, compared to the experimental investigations in Section 2, raises the question of the extent to which this increase influences the electrode properties negatively. Indeed, a reduction in adhesion can be expected at least to some extent through this measure. The decrease in adhesion with increasing drying rate has been demonstrated

in prior research.^[17] Nevertheless, the same study also reveals that with an infrared-adjusted drying rate of $2.5 \text{ g m}^{-2} \text{ s}^{-1}$, comparable adhesion as with one-sided, purely convective drying at a drying rate of only $0.8 \text{ g m}^{-2} \text{ s}^{-1}$ can be achieved.^[17] It can therefore be concluded that with the described procedure, at least equivalent electrodes can be expected as with a purely convective drying process, despite a clearly increased drying rate in the critical structure formation interval.

For a quantitative illustration of the savings potential, the required drying time is plotted in Figure 7 as a function of the share of time dried at the specified HDR. Moreover, the drying rate averaged from the process combination over the entire drying process is plotted on the secondary x-axis. Figure 7 illustrates that the required drying time can be significantly reduced with increasing intervals in which drying is done at HDR. Consequently, single-stage drying with 100% LDR requires about 69 s of drying time, while drying with 100% HDR will only require 17 s. However, to maintain the quality of the electrodes according to the findings explained in Section 2, drying must be carried out gently in specific sections, which rules out drying exclusively at HDR in combination with good electrode quality. Accordingly, the required drying time by adhering to the optimum transition times calculated with Equation (4) and the critical volume fractions given in Table 1 for the two- and three-stage processes are shown as bars in the diagram with the saved drying time indicated for each multistage process variant.

For a two-stage drying process, 33% drying time can be saved when 16% of the total drying time is carried out at HDR, leading to an average overall drying rate of $3.7 \text{ g m}^{-2} \text{ s}^{-1}$. 53% drying time can be saved with a three-stage process in comparison to single-stage drying with the lower drying rate, when 38% of the total drying time is carried out at HDR, corresponding to an average overall drying rate of $5.3 \text{ g m}^{-2} \text{ s}^{-1}$.

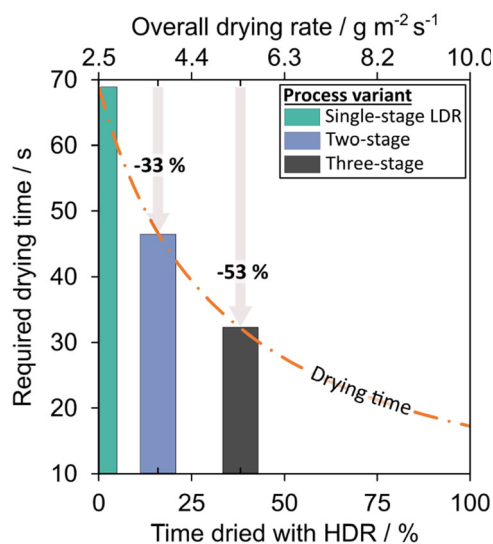


Figure 7. Required drying time as a function of the share of the total drying time dried at HDR respectively the average drying rate for drying of an aqueous graphite electrode with an initial solvent content of 57 wt% and a dry area weight of 130 g m^{-2} for a HDR of $10 \text{ g m}^{-2} \text{ s}^{-1}$ and a LDR of $2.5 \text{ g m}^{-2} \text{ s}^{-1}$.

The values given in percentages do not only indicate the savings potential in terms of drying time, but also the reduction of dryer line length when using a roll-to-roll process with continuous coating. The required dryer length for a complete drying in roll-to-roll systems can be calculated for a given coating speed u_{coat} , specified drying rates and slurry parameters. When applying multistage drying profiles, the length of the individual drying sections $L_{\text{Section},i}$ must be determined beforehand. These can be specified on the basis of the drying rate \dot{m}_i in the respective drying section and the desired solvent content at the end of the section $x_{S,i,\text{out}}$ using Equation (7):

$$L_{\text{Section},i} = \frac{u_{\text{coat}} m_{\text{El}}}{\dot{m}_i} \left(\frac{x_{S,i,\text{out}}}{1 - x_{S,i,\text{out}}} - \frac{x_{S,i,\text{in}}}{1 - x_{S,i,\text{in}}} \right) \quad (7)$$

For the first zone, the solvent content at the inlet $x_{S,i,\text{in}}$ is the initial solvent content of the electrode slurry in wt%. For the next zone the solvent content at the dryer zone inlet $x_{S,i+1,\text{in}}$ equals to the solvent content at the outlet of the previous zone $x_{S,i,\text{out}}$ and so forth. The solvent content at the end of the last section equals zero, although a small amount of bound solvent in a real production has to be removed in a postdrying process. The total dryer length L_{Dryer} can be calculated with Equation (8):

$$L_{\text{Dryer}} = \sum_i^n L_{\text{Section},i} \quad (8)$$

Even though the described method allows the application of an arbitrary number of drying zones, the results in Section 2 suggest

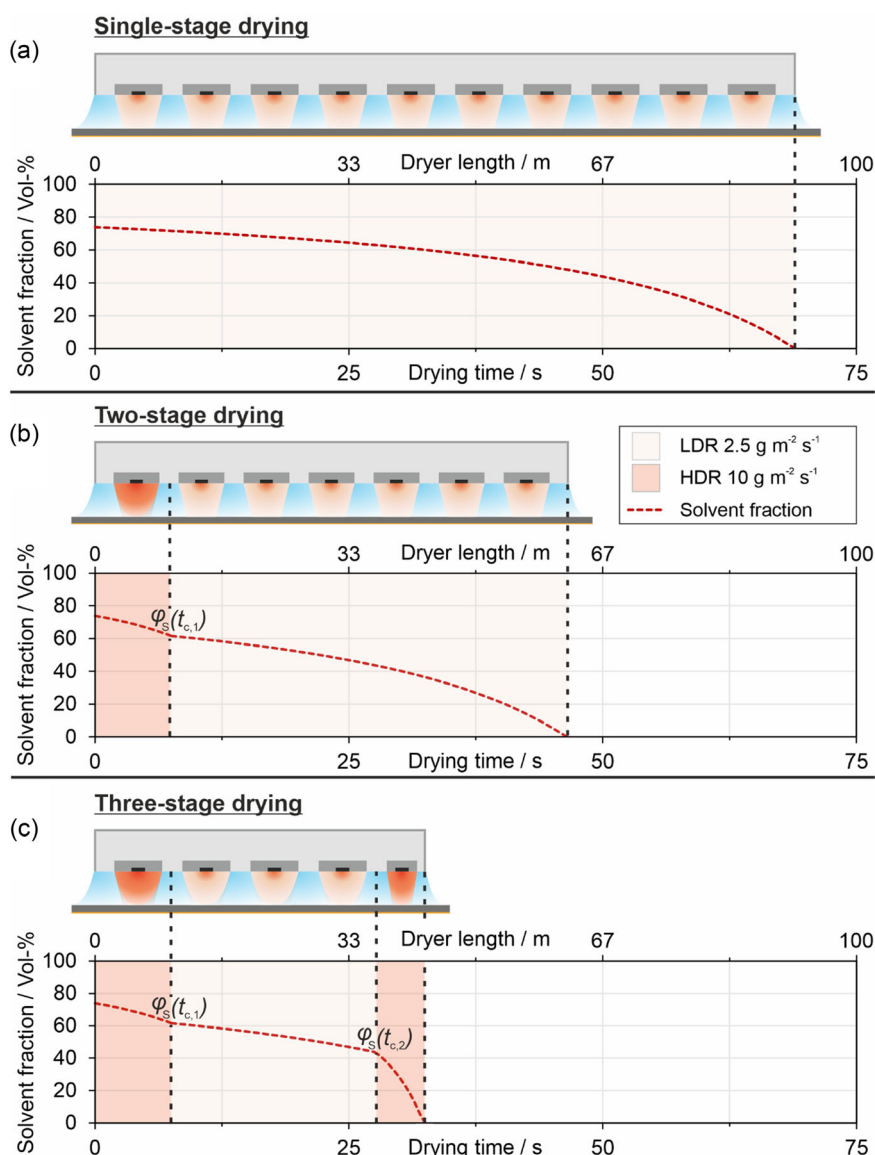


Figure 8. a) Comparison of a single-stage, b) two-stage, and c) three-stage drying process of an aqueous graphite anode with a dry area weight of 130 g m^{-2} , an initial solvent content of 57 wt% and a production speed of 80 m min^{-1} . The dryer lengths including infrared dryers for each process variant are shown schematically, as well as the progress of the volume fraction of solvent as a function of the dryer length and the drying time.

to subdivide the drying process roughly into three periods, in which the drying rate is adjusted individually (inlet and outlet as well as heating and cooling processes neglected). In **Figure 8**, the required drying times and dryer lengths for the different process variants are compared for a production speed of 80 m min^{-1} in a roll-to-roll process. For each process variant a schematic dryer module including infrared modules, as well as the progression of solvent volume fraction along the dryer length and the drying time is shown. Depending on the process variant, the length of a dryer section is determined by applying the critical solvent contents in Equation (7).

The drying times indicated in the diagrams correspond to those in Figure 7. For the resulting dryer lengths, the same savings in percent as for the drying times are obtained using the multistage processes. With the electrode parameters specified herein and the predefined line speed, the dryer length is about 92 m for the single-stage process, 62 m for the two-stage process and 43 m for the three-stage process. Without conducting a detailed economic evaluation, it may be assumed that a reduction in dryer length, enabled by adopting multistage drying profiles, in addition to the considerable savings of production space, holds potential for reducing the investment costs of a dryer line. Based on data by Schünemann et al. investment costs of $\approx \text{€}0.65$ million per 10 m dryer length can be estimated for purely convective dryers.^[5] Unfortunately, to the authors' current knowledge, no substantiated data are available for the investment and operating costs of infrared radiators in the production scenario described. Although electrodes with excellent properties can be produced at HDRs using pure infrared drying, attention must be drawn to the fact that for application in a production process under continuous operation, the removal of solvent from the ambient air must not be disregarded. The accumulation of solvent in the ambient air could lead to long-term changes in drying rates and electrode temperatures due to a shifting concentration gradient of solvent between the drying electrode surface and the ambient air as well as the possibility of condensing the airborne solvent onto dryer components. The impact of solvent loading in the ambient air (dew point) on the drying process was described in several works.^[12,17] For no-aqueous solvent-based processes, the maintenance of a non-explosive atmosphere (for example, by complying with the ATEX directives which are widely applied in the European Union) is an additional mandatory requirement. However, this must also remain valid for any conventional drying process without heat input by radiation. Concluding this section, it becomes evident that the economic classification and the sustainable integration of heat input through radiation represents a crucial measure for electrode production that should be investigated in further detail.

5. Conclusion

In the present study, a multistage drying concept was established by identifying characteristic drying periods that can be used to significantly accelerate the drying of the investigated anode slurry without negatively affecting the electrode properties. The approach is based on some of our previously published findings for a different solvent and binder system, as well as a different drying methodology and drying rates. The concept proposed in

this study was validated through drying experiments on water-based graphite anodes using a two- and three-stage NIR drying process by comparing the adhesion strength, which is representative of the electrode quality, for different process variants. Two-stage drying experiments were used in which drying was first performed at a higher drying rate of $6 \text{ g m}^{-2} \text{ s}^{-1}$ and then, after a variable transition time, at a lower drying rate of $0.75 \text{ g m}^{-2} \text{ s}^{-1}$ to evaluate the critical drying range within which a high drying rate leads to adhesion degradation due to binder migration. For the material system used, the experimental investigations revealed a critical interval between 61 and 43 vol% solvent. An essential observation in this context is that the onset of the critical region for structure formation is localized before the theoretical end of film shrinkage and concomitant formation of the final porous electrode structure. This partially aligns with previously published results, indicating that the critical period is present when the final thickness is reached, i.e., at the formation of the final porosity, although it may be localized earlier for high drying rates.

Three-stage drying experiments were conducted to successfully validate the model and demonstrate that the underlying mechanisms are applicable to both NIR drying and a water-based anode with CMC/SBR binder.

The time-saving potential of multistage drying concepts was demonstrated on the basis of analytical calculations. In the example shown, the savings potential amounts to a reduction of the drying time and dryer length by 60% without negative effects on the electrode properties, if the three-stage drying process is applied appropriately. Selected electrodes produced with the reference processes for slow and fast drying, as well as two- and three-stage drying profiles, were subjected to electrochemical performance tests. In essence, the studies demonstrate that despite accelerated drying using multistage profiles, no negative impact on cell performance is associated, whereas rapid drying in a single-stage process results in poor performance.

Furthermore, the findings were theoretically scaled up to production scale, and the required drying time and dryer length for single-, two- and three-stage processes were demonstrated. At a specified throughput speed of 80 m min^{-1} , the key conclusion for the parameters chosen is that the drying length can be reduced from 92 to 43 m by using a multistage process with individually set drying rates in three drying sections. Notably, this approach holds promise in unlocking substantial potential, presumably without compromising the electrode's properties.

6. Experimental Section

Electrode Composition and Slurry Preparation: For slurry preparation, CMC (Sunrose MAC500LC, Nippon Paper Industries Co., Ltd., Japan) was dissolved in water at ambient temperature in a laboratory stirrer for 1 h at 500 rpm. Graphite particles (SMGA, Hitachi Chemical Co. Ltd., Japan) and carbon black (Super C65, Timcal SA, Switzerland) were mixed in a dry mixing step for 10 min at 300 rpm in a dissolver mixer (Dispermat CN10, VMA Getzmann GmbH Verfahrenstechnik, Germany), which features a vessel with a diameter of 81 mm while the stirring disc has a diameter of 70 mm. Solids were added to the CMC water solution in three thickening steps while stirring the mixture at 500 rpm. While the temperature of the vessel was temperature-controlled by cooling water, degassing was executed and the slurry was dispersed at 1500 rpm for 45 min. In a last step, SBR binder (Zeon Europe GmbH, Japan) was

Table 3. Composition of the dry electrode and the electrode slurry.

Component	Dry mass fraction [wt%]	Wet mass fraction [wt%]
Graphite	93.00	40.00
Carbon black	1.40	0.60
CMC	1.87	0.80
SBR	3.73	1.60
Water	–	57.00

added and the dispersion was mixed at 500 rpm for 10 min. The resulting mass composition of the components is listed in **Table 3**.

Coating and Drying: For the coating step, 10 μm thick copper foil (Civen Metal Material Co. Ltd., China) was used as a substrate. To realize a homogeneous surface and guarantee defined coating conditions, the foil was fixed in a tensioned frame and placed on a flat coating plate equipped with a vacuum groove suction. A doctor blade (UA2000.100, Proceq SA, Switzerland) was used to apply films of defined thickness and geometry. For coating, the doctor blade was moved by a linear actuator at a speed of 50 mm s^{-1} , while the coating gap was adjusted to $265\text{ }\mu\text{m}$ to achieve a dry area weight of $\approx 130\text{ g m}^{-2}$. To obtain the same electrode geometry in each experiment, a $20\text{ }\mu\text{m}$ thick polyethylene terephthalate (PET) stencil with a cut-out area of $90\text{ by }90\text{ mm}$ was used during the coating process. The stencil was removed after the coating prior to drying. The procedure corresponds to that used in a previous work.^[17]

After coating, the electrodes were dried with energy input by infrared radiation using a NIR120 M4 module (adphos Innovative Technologies GmbH, Germany), emitting in a wavelength around $1\text{ }\mu\text{m}$ with a maximum power of 3.3 kW and an irradiation area of $\approx 0.042\text{ m}^2$, which was already used in a previous study.^[17] An infrared transmissive glass panel was installed below the module to deflect the cooling air of the radiation module, allowing isolated energy input by NIR radiation during drying. In the drying experiments, the input power $P_{\text{el,IR}}$ of the module was varied between 550 and 2130 W to adjust drying rates of 0.75 and $6\text{ g m}^{-2}\text{ s}^{-1}$. For drying, the module was positioned at a distance of 120 mm above the electrode coating and remained enabled until the coating was sufficiently dried, as indicated by a rapid rise of electrode temperature. The drying module was switched off when the measured temperature reached about $120\text{ }^\circ\text{C}$. Thermographic images of characterization tests for both settings are given in the Figure S4, Supporting Information.

As the electrode-carrying tensioned frame was mounted on a rack, a thermocouple was attached to the underside of the copper to observe the temperature for all drying experiments with subsequent measurement of electrode adhesion. The procedure corresponds to that used in a previous work.^[17]

For the production of flawless electrodes for the cell tests in the required format (Section 3), the attachment of a thermocouple was omitted. To identify the end point of the drying process, an infrared camera (PI 400, optris GmbH, Germany) was used instead and, as the average temperature of the electrode area increased beyond $\approx 120\text{ }^\circ\text{C}$, the energy supply by NIR radiation was terminated. The drying settings in terms of input power and distance of the NIR module were selected analogously to the drying tests with subsequent adhesion characterization.

Electrode Characterization: The porosity was calculated from the area weight m_{El} and the layer thickness h_{El} using the density of the dry mixture of the electrode's components $\bar{\rho}_{\text{El}}$ with Equation (9):

$$\varepsilon_{\text{El}} = 1 - \frac{m_{\text{El}}}{\bar{\rho}_{\text{El}} h_{\text{El}}} \quad (9)$$

Adhesion strength was measured using a universal testing machine type AMETEK LS1 (Lloyd Instruments Ltd., UK) with a 90° peeling device and a 10 N load-cell. Specimens of 28 mm width were tested, cut perpendicular to the coating direction, using three specimens per electrode. The mean value and the standard deviation were determined.

Evaluation of Fit Parameters to Adhesion Measurement Data from Two-Stage Transition Experiments: To adjust a suitable fit function representing the development of adhesion in multistage drying considering the transition time, the method described by Jaiser et al. was applied.^[9] Here, a 4PL regression for the adhesion as a function of the transition time based on four fit parameters was used. The fit F given in Equation (10) is plotted over the transition time and fitted to the measured adhesion values using the least squares method varying the parameters A_1 , A_2 , t_0 , and p :

$$F = \frac{A_1 - A_2}{1 + \left(\frac{t}{t_0}\right)^p} \quad (10)$$

By applying a tangent at the inflection point of the fit and inserting horizontal lines at the level of the fit parameters A_1 and A_2 , the periods delimiting the characteristic time intervals during drying on the x-axis are determined from the resulting intersection points. From the intersection point of the tangent with the horizontal on the plane of A_1 , $t_{c,1}$ is read while from the intersection point with the horizontal on the plane of A_2 , $t_{c,2}$ is read. A detailed description of the procedure is published in ref. [9].

Coin and Pouch Cell Preparation and Electrochemical Characterization: The cell preparation and testing procedure correspond to the description by Smith et al. in ref. [35]. Coin cell assembly was performed in an argon-filled glovebox. CR2032 cells (Hohsen Corp., Japan) were used with lithium chips (MTI Corporation, USA, 15.6 mm in diameter, thickness of $250\text{ }\mu\text{m}$) against graphite anodes with diameters of 14 mm . A 1-molar LiPF_6 in a 50/50 (w/w) mixture of ethylene carbonate (EC) and dimethyl carbonate (DMC), with 3 wt% of vinylene carbonate (VC, Gotion High-Tech Co., Ltd.) was used as an electrolyte. The electrolyte volume was $350\text{ }\mu\text{L}$. The metal spacer thickness was 1 mm and the separator was glass fiber type GF/D (Whatman, Inc., UK). Before electrochemical measurements, the cells were stored at $40\text{ }^\circ\text{C}$ overnight for sufficient wetting. Cells underwent formation using C/50 charge rate, with subsequent cycles at a c-rate of C/10 with a total of four complete cycles (note that at charging with C/10 a CV-phase was applied until the current dropped below C/20). The overall voltage window was set from 0.005 to 1.000 V . The assembly of pouch cells took place in a dry environment (dew point $-60\text{ }^\circ\text{C}$). The dried anodes were cut to a size of $5.2\text{ by }5.2\text{ cm}$. As for the cathodes, they consist of commercial NMC811 material (96% NMC811, 2% conductive carbon type Denka Black, 2% PVDF) and measure $5.0\text{ by }5.0\text{ cm}$. A commercial ceramic-coated PET fabric separator with dimensions of $5.5\text{ by }5.5\text{ cm}$ was utilized. To prepare the electrodes and separators for assembly, the components were dried under reduced pressure at 130 and $180\text{ }^\circ\text{C}$, respectively, for 24 h . The cells were constructed with one double-side-coated cathode and one single-side-coated anode separated by one sheet of separator in a pouch bag with $700\text{ }\mu\text{L}$ electrolyte (1-molar LiPF_6 in a 50/50 (w/w) mixture of EC and DMC, with 3 wt% of vinylene carbonate VC). After filling, the cells were sealed under reduced pressure and stored overnight at $40\text{ }^\circ\text{C}$ to ensure proper wetting of the separator and electrodes. Pouch cell testing was conducted with BaSyTec CTS LAB instruments. During the tests, the cells were stored in climate chambers at a temperature of $25\text{ }^\circ\text{C}$ ($\pm 0.1\text{ }^\circ\text{C}$) and mounted in a four-point contacting setup. The practical capacity of the double-side-coated cathodes was $\approx 4.0\text{ mAh cm}^{-2}$ per side, so 1C corresponds to a current density of 4.0 mA cm^{-2} . As the graphite anodes showed capacities of $\approx 4.4\text{ mAh cm}^{-2}$, sufficient anode to cathode capacity balancing was achieved. During the formation step, four cycles were applied. Charging was performed with constant current (CC) at C/10 until a voltage of 4.2 V was reached, followed by charging at constant voltage (CV) until the current dropped below C/20. Discharge was carried out using CC at C/10. Finally, the cells were charged to 3.7 V . An asymmetric rate test was subsequently conducted. During this test, charging was carried out at C/2 at CC with a CV phase with a cutoff of $<C/20$. The discharge rates varied from C/2 to 5C. To assess degradation resulting from the rate testing, a C/2 discharge was included at the end of the test procedure. Two full cycles were applied for each c-rate.

Supporting Information

Supporting Information is available from the Wiley Online Library or from the author.

Acknowledgements

The authors would like to thank Sven Leuthner and Olivia Wiegand for cell preparation. The authors would like to acknowledge financial support by the Federal Ministry of Education and Research (BMBF) via the ProZell cluster-project “Epic” (grant number: 03XP0295A) and by the German Research Foundation (DFG) under Germany’s Excellence Strategy – EXC 2154 – Project number 390874152 (POLiS Cluster of Excellence). This work contributes to the research performed at the Center for Electrochemical Energy Storage Ulm-Karlsruhe (CELEST).

Open Access funding enabled and organized by Projekt DEAL.

Conflict of Interest

The authors declare no conflict of interest.

Data Availability Statement

The data that support the findings of this study are available from the corresponding author upon reasonable request.

Keywords

adhesion, binder migration, electrode drying, lithium-ion battery electrodes, near-infrared

Received: October 10, 2023

Revised: January 26, 2024

Published online:

- [1] L. Mauler, F. Duffner, J. Leker, *Appl. Energy* **2021**, *286*, 116499.
- [2] R. Diehm, M. Müller, D. Burger, J. Kumberg, S. Spiegel, W. Bauer, P. Scharfer, W. Schabel, *Energy Technol.* **2020**, *8*, 2000259.
- [3] D. L. Wood, J. D. Quass, J. Li, S. Ahmed, D. Ventola, C. Daniel, *Drying Technol.* **2018**, *36*, 234.
- [4] M. Baunach, S. Jaiser, S. Schmelzle, H. Nirschl, P. Scharfer, W. Schabel, *Drying Technol.* **2016**, *34*, 462.
- [5] J.-H. Schünemann, *Modell zur Bewertung der Herstellkosten von Lithiumionenbatteriezellen*, Zugl.: Braunschweig, Techn. Univ., Diss., Sierke, Göttingen **2015**.
- [6] D. Küpper, K. Kuhlmann, S. Wolf, C. Pieper, G. Xu, J. Ahmad, <https://www.bcg.com/publications/2018/future-battery-production-electric-vehicles> (accessed: May 2023).
- [7] M. Thomitzek, N. von Drachenfels, F. Cerdas, C. Herrmann, S. Thiede, *Procedia CIRP* **2019**, *80*, 126.
- [8] S. Jaiser, N. Sanchez Salach, M. Baunach, P. Scharfer, W. Schabel, *Drying Technol.* **2017**, *35*, 1807.
- [9] S. Jaiser, M. Müller, M. Baunach, W. Bauer, P. Scharfer, W. Schabel, *J. Power Sources* **2016**, *318*, 210.

- [10] M. Müller, L. Pfaffmann, S. Jaiser, M. Baunach, V. Trouillet, F. Scheiba, P. Scharfer, W. Schabel, W. Bauer, *J. Power Sources* **2017**, *340*, 1.
- [11] J. Klemens, L. Schneider, E. C. Herbst, N. Bohn, M. Müller, W. Bauer, P. Scharfer, W. Schabel, *Energy Technol.* **2022**, *10*, 2100985.
- [12] J. Kumberg, M. Müller, R. Diehm, S. Spiegel, C. Wachsmann, W. Bauer, P. Scharfer, W. Schabel, *Energy Technol.* **2019**, *7*, 1900722.
- [13] B. Westphal, H. Bockholt, T. Gunther, W. Haselrieder, A. Kwade, *ECS Trans.* **2015**, *64*, 57.
- [14] S. Jaiser, J. Kumberg, J. Klaver, J. L. Urai, W. Schabel, J. Schmatz, P. Scharfer, *J. Power Sources* **2017**, *345*, 97.
- [15] R. Morasch, J. Landesfeind, B. Suthar, H. A. Gasteiger, *J. Electrochem. Soc.* **2018**, *165*, A3459.
- [16] J. Klemens, L. Schneider, D. Burger, N. Zimmerer, M. Müller, W. Bauer, H. Ehrenberg, P. Scharfer, W. Schabel, *Energy Technol.* **2023**, *11*, 2300338.
- [17] A. Altvater, T. Heckmann, J. C. Eser, S. Spiegel, P. Scharfer, W. Schabel, *Energy Technol.* **2022**, *11*, 2200785.
- [18] J. Kumberg, W. Bauer, J. Schmatz, R. Diehm, M. Tönsmann, M. Müller, K. Ly, P. Scharfer, W. Schabel, *Energy Technol.* **2021**, *9*, 2100367.
- [19] J. Klemens, D. Burger, L. Schneider, S. Spiegel, M. Müller, N. Bohn, W. Bauer, H. Ehrenberg, P. Scharfer, W. Schabel, *Energy Technol.* **2023**, *11*, 2300338.
- [20] C. Busson, M.-A. Blin, P. Guichard, P. Soudan, O. Crosnier, D. Guyomard, B. Lestriez, *J. Power Sources* **2018**, *406*, 7.
- [21] S. Jaiser, A. Friske, M. Baunach, P. Scharfer, W. Schabel, *Drying Technol.* **2017**, *35*, 1266.
- [22] T. Metzger, E. Tsotsas, *Drying Technol.* **2005**, *23*, 1797.
- [23] N. Vorhauer, Y. J. Wang, A. Kharaghani, E. Tsotsas, M. Prat, *Transp. Porous Media* **2015**, *110*, 197.
- [24] S. Jaiser, L. Funk, M. Baunach, P. Scharfer, W. Schabel, *J. Colloid Interface Sci.* **2017**, *494*, 22.
- [25] J. Kumberg, M. Baunach, J. C. Eser, A. Altvater, P. Scharfer, W. Schabel, *Energy Technol.* **2021**, *9*, 2100013.
- [26] H. Yamamoto, H. Mori, in *Lithium-Ion Batteries. Science and Technologies* (Eds: M. Yoshio, R. J. Brodd, A. Kozawa), Springer, New York, NY **2009**, pp. 1–17.
- [27] S. H. Sung, S. Kim, J. H. Park, J. D. Park, K. H. Ahn, *Materials* **2020**, *13*, 4544.
- [28] S. Fink, D. Demir, M. Börner, V. Göken, C. Vedder, *World Electr. Veh. J.* **2023**, *14*, 255.
- [29] S. Wolf, N. Schwenzer, T. Tratz, V. Göken, M. Börner, D. Neb, H. Heimes, M. Winter, A. Kampker, *World Electr. Veh. J.* **2023**, *14*, 281.
- [30] Y. Nishi, *J. Power Sources* **2001**, *100*, 101.
- [31] J. Park, S. Suh, S. Tamulevičius, D. Kim, D. Choi, S. Jeong, H.-J. Kim, *Nanomaterials* **2022**, *12*, 2625.
- [32] F. J. Günter, N. Wassiliadis, *J. Electrochem. Soc.* **2022**, *169*, 30515.
- [33] R. Gordon, A. Smith, *J. Energy Storage* **2023**, *72*, 108200.
- [34] N. Wassiliadis, M. Steinsträßer, M. Schreiber, P. Rosner, L. Nicoletti, F. Schmid, M. Ank, O. Teichert, L. Wildfeuer, J. Schneider, A. Koch, *eTransportation* **2022**, *12*, 100167.
- [35] A. Smith, P. Stüble, L. Leuthner, A. Hofmann, F. Jeschull, L. Mereacre, *Batteries Supercaps* **2023**, *6*, e20230008.